

Quantized Conductance and Large g -Factor Anisotropy in InSb Quantum Point Contacts

Fanming Qu,[†] Jasper van Veen,[†] Folkert K. de Vries,[†] Arjan J. A. Beukman,[†] Michael Wimmer,[†] Wei Yi,[‡] Andrey A. Kiselev,[‡] Binh-Minh Nguyen,[‡] Marko Sokolich,[‡] Michael J. Manfra,[§] Fabrizio Nichele,^{||} Charles M. Marcus,^{||} and Leo P. Kouwenhoven^{*,†}

[†]QuTech and Kavli Institute of Nanoscience, Delft University of Technology, 2600 GA Delft, The Netherlands

[‡]HRL Laboratories, 3011 Malibu Canyon Road, Malibu, California 90265, United States

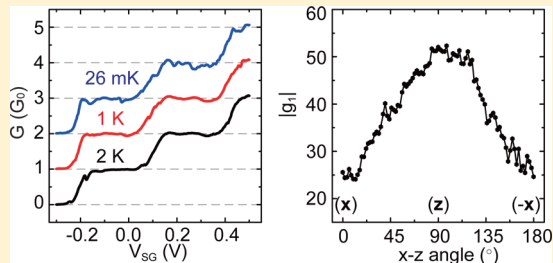
[§]Department of Physics and Astronomy, and Station Q Purdue, School of Electrical and Computer Engineering, School of Materials Engineering, Purdue University, West Lafayette, Indiana 47907, United States

^{||}Center for Quantum Devices, Niels Bohr Institute, University of Copenhagen, Copenhagen 1017, Denmark

Supporting Information

ABSTRACT: Because of a strong spin–orbit interaction and a large Landé g -factor, InSb plays an important role in research on Majorana fermions. To further explore novel properties of Majorana fermions, hybrid devices based on quantum wells are conceived as an alternative approach to nanowires. In this work, we report a pronounced conductance quantization of quantum point contact devices in InSb/InAlSb quantum wells. Using a rotating magnetic field, we observe a large in-plane ($|g_{\parallel}| = 26$) and out-of-plane ($|g_{\perp}| = 52$) g -factor anisotropy. Additionally, we investigate crossings of subbands with opposite spins and extract the electron effective mass from magnetic depopulation of one-dimensional subbands.

KEYWORDS: InSb quantum well, quantum point contact, g -factor anisotropy, electron effective mass, conductance quantization



Among the binary III–V semiconductors, InSb has the smallest effective mass and the highest room-temperature mobility.¹ It further exhibits a strong spin–orbit interaction (SOI) and the largest Landé g -factor ($|g| = 51$ for the bulk) due to the strong coupling between the conduction band and the valence band resulting from the small energy gap.^{1–3} Besides the continuously increasing interest in its various applications in spintronics,⁴ InSb has been extensively investigated for Majorana fermions and topological quantum computing (TQC).^{5,6} Applying a magnetic field perpendicular to the spin–orbit field of a nanowire opens a Zeeman energy gap and creates one-dimensional (1D) helical states.⁷ Furthermore, when a superconducting gap is induced through the proximity effect, a 1D topological superconductor can form and Majorana zero modes (MZMs) emerge at the boundaries of this topological phase. InSb nanowires played an important role in the first experimental signature of MZMs.⁸ While rapid progress has been achieved based on InSb and InAs nanowires,^{9–12} further investigation of the non-Abelian properties and the unique fusion rules of MZMs requires more complex device designs.^{13–15} Although crossed nanowires have been developed,¹⁶ simultaneously applying magnetic fields parallel to different branches of such nanocross is difficult to realize, since this requires, for example, an “H” bar with parallel arms. Moreover, the scalability of nanowire systems for TQC can be challenging. Therefore, a “top-down” approach by

fabricating 1D or network structures starting from a two-dimensional (2D) quantum well system is a promising alternative route.

InSb quantum wells have several important advantages over InSb nanowires. The mobility can exceed $200\,000\text{ cm}^2/(\text{V s})$,^{17–19} corresponding to a mean free path larger than $1.4\text{ }\mu\text{m}$. To realize 1D helical states, it is crucial to optimize the potential profile for transport detection,²⁰ which can be tailored through geometry design based on electrostatic modeling. In addition, the 2D electron gas (2DEG) functions as ideal contacts that naturally solves the interface problem for nanowires.²¹ Although the calculated and reported Rashba SOI parameter α ranging $0.03\text{--}0.15\text{ eV\AA}$ ^{22–27} is smaller than that reported in nanowires,^{3,28} a 2D heterostructure enables tuning of SOI strength^{22,23,25–27,29} by engineering asymmetric doping, barrier modulation, and also electrical gating. The confinement of 1D structures defined on an InSb 2DEG may enhance α toward the values for nanowires. Together with the flexibility of complex device designs, these advantages motivate a detailed investigation of 1D structures based on InSb quantum wells. However, the successful gate depletion of InSb 2DEG was achieved only recently after solving the gate

Received: August 5, 2016

Revised: October 25, 2016

Published: November 2, 2016

leakage problem.^{19,30} While 1D ballistic transport has been established in InSb nanowires and nanosails lately,^{31,32} only one work reported an observation of quantized conductance in quantum point contacts (QPCs) on an InSb 2DEG.³³ Detailed transport properties including g -factors and the electron effective mass in 1D structures confined on InSb quantum wells are yet to be established. In this work, we demonstrate ballistic transport through QPCs in an InSb 2DEG. In a rotating magnetic field, the Zeeman spin splitting is investigated and a large in-plane and out-of-plane g -factor anisotropy is observed. Furthermore, crossings of subbands with opposite spins are studied and the electron effective mass is deduced using magnetic depopulation.^{34,35}

The InSb/InAlSb heterostructure used in this work is grown on a GaAs (100) substrate using a fully relaxed $\text{In}_{1-x}\text{Al}_x\text{Sb}$ buffer ($x = 0.08$). The quantum well consists of a 30 nm InSb layer sandwiched between $\text{In}_{1-x}\text{Al}_x\text{Sb}$ barriers. Single side Si δ -doping sits 20 nm above the InSb layer in the top barrier. Details of the material growth and a full gate depletion of the 2DEG in Hall bar devices with HfO_2 as dielectric have been reported earlier.¹⁹ To fabricate the QPC device studied here, as shown in Figure 1a, a narrow constriction (~ 280 nm wide) on a $20 \mu\text{m}$ wide mesa is wet etched ~ 100 nm deep, followed by sputtering a 100 nm thick Si_3N_4 dielectric layer, and evaporating a 100 nm wide Ti/Au top gate. The InSb 2DEG at both sides of the constriction functions as two in-plane side

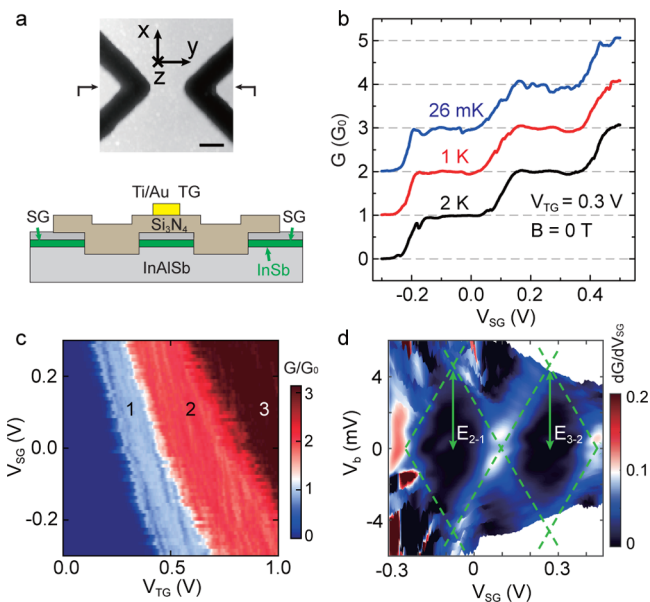


Figure 1. Conductance quantization in etch-defined InSb QPCs. (a) Image and schematics of the etch-defined QPC device. The top panel shows an atomic force microscope image of the constriction after a wet etch (before depositing Si_3N_4 and Ti/Au layers) with the black region being ~ 100 nm deep. The scale bar is 200 nm. The axes illustrate the vector magnet orientations. The bottom panel displays the cross-section of the device along the plane marked by the two arrows in the top panel. The constriction is controlled by two etch-defined in-plane SG and a 100 nm wide TG. (b) Differential conductance G versus side gate voltage V_{SG} curves at a fixed top gate voltage $V_{\text{TG}} = 0.3$ V for different temperatures. Traces are offset by $1G_0$ ($G_0 = 2e^2/h$) for clarity. (c) G as a function of both V_{TG} and V_{SG} . (d) Numerically calculated transconductance dG/dV_{SG} as a function of V_{SG} and dc bias voltage V_b at $V_{\text{TG}} = 0.3$ V. The green dashed lines are guides to the eye and the green solid arrows indicate the subband spacings.

gates (SG). The ohmic contacts, located $>20 \mu\text{m}$ away from the QPC, are formed by etching into the InSb layer using an argon ion etch and in situ deposition of Ti/Au layers. In addition, we also fabricated fully gate-defined QPCs in which instead of etching the constriction is defined by two split Ti/Au side gates on top of Si_3N_4 dielectric and a global Ti/Au top gate on a second Si_3N_4 layer (see Supporting Information Figure S1).

Transport measurements are carried out on the two types of InSb QPCs in both a cryo-free dilution refrigerator with a 6-2-1 T vector magnet and a ^3He system with a single axis magnet of 9 T. Standard low-frequency lock-in techniques are employed in a configuration of two-terminal or four-terminal measurement. Series resistances from the wires, measurement equipment and adjacent InSb 2DEG have been subtracted to match the quantized conductance for the data reported below, unless otherwise stated. For the source-drain bias spectroscopy, the voltage drop on the QPC is also corrected accordingly. Hall bar devices with Si_3N_4 as dielectric are characterized before performing the QPC measurements (see Supporting Information Figure S2). By a comparison of the two types of QPCs, we find that the etch-defined QPC shows pronounced quantized conductance plateaus at zero magnetic field, while the fully gate-defined type requires a small perpendicular magnetic field to suppress backscattering and interference. Therefore, we focus on the former in the following and briefly present the results on the latter in the Supporting Information Figure S1.

Differential conductance $G = dI/dV = I_{\text{ac}}/V_{\text{ac}}$ is measured by applying a small ac excitation voltage V_{ac} with or without a dc bias voltage V_b and measuring the ac current I_{ac} . Figure 1b shows G as a function of side gate voltage V_{SG} with a fixed top gate voltage $V_{\text{TG}} = 0.3$ V at different temperatures. Quantized conductance plateaus at nG_0 are observed resulting from the ballistic transport in the 1D constriction, where $n = 1, 2,$ and 3 , and $G_0 = 2e^2/h$ (h is the Planck constant and e the elementary charge). At mixing chamber temperature $T = 26$ mK, small conductance fluctuations indicate finite backscattering and interference processes around the QPC. The rest of the data reported below are all measured at 26 mK. As shown in Figure 1c, G can be controlled by both top gate and side gates, confirming their proper functioning. Figure 1d displays the numerically calculated derivative of G with respect to side gate voltage, that is, the transconductance dG/dV_{SG} , versus V_{SG} and V_b . (Raw data of G versus V_{SG} and V_b is shown in Figure S3b of the Supporting Information.) As indicated by the green solid arrows, subband spacings E_{2-1} and E_{3-2} of ~ 4.6 meV are roughly equal (E_{i-j} represents the energy spacing between the i th and j th subbands where i and j are an integer), suggesting a near-parabolic confinement potential.

We further examine the spin splitting of the 1D subbands in a magnetic field. Figure 2a shows G as a function of V_{SG} and B_x (along current flow) where n can now assume half integer values. As B_x increases from 0 T, half integer plateaus resulting from Zeeman spin splitting appear and widen in V_{SG} while the integer plateaus narrow down. The evolution of spin resolved subbands in B_x is illustrated in the right panel of Figure 2b ignoring SOI. At $B_x = 3$ T, as shown by the green curve in the left panel of Figure 2b, only half integer plateaus survive when the spin-down band from the i th subband ($i\downarrow$) crosses the spin-up band from the $(i+1)$ th subband ($(i+1)\uparrow$). When $B_x > 3$ T, after the crossing of the spin split subbands, the spin-up bands $1\uparrow$ and $2\uparrow$ are the lowest two bands in energy. At $B_x = 4$ T, the integer plateaus are restored but are now fully spin polarized for $1G_0$. Note that a combination of a large g -factor and the modest

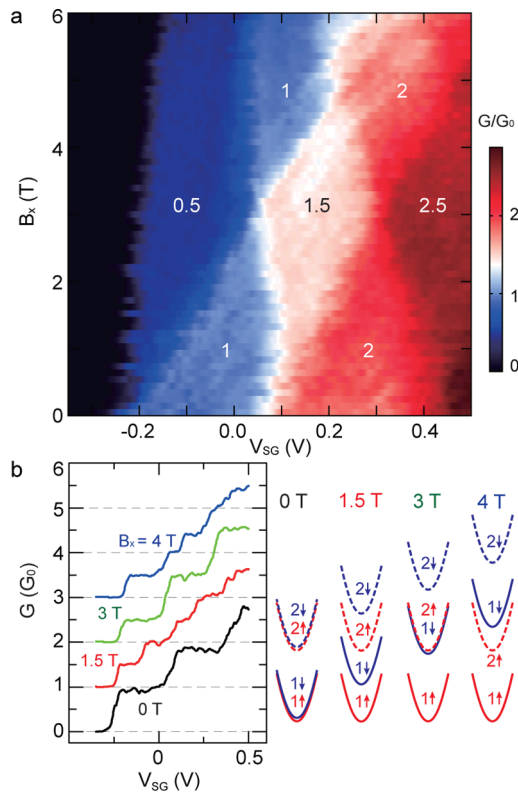


Figure 2. Crossings of electron subbands with opposite spins. (a) G versus V_{SG} and B_x (along current flow) at $V_{TG} = 0.3$ V with numbers n labeling quantized conductance at nG_0 . (b) The left panel shows line cuts taken from (a) at different magnetic fields. Traces are offset by $1G_0$ for clarity. The right panel displays band dispersions at different B_x , sketching the evolution of the spin resolved subbands.

subband separation enables such clear crossing at a moderate magnetic field.^{36,37} When two 1D subbands of opposite spins cross, a spontaneous spin splitting and the emergence of the so-called 0.7 analog at the 1.5 plateau have been reported in GaAs 2DEG,³⁶ which, as well as the $0.7G_0$ feature, are absent here in our InSb QPCs but require further investigation.

At large $B_z > 1$ T (out-of-plane), as shown in Figure 3a, in contrast to the case of B_x all plateaus widen due to Zeeman splitting and magnetic depopulation of 1D subbands, as will be discussed below. For the case of B_y (in-plane but perpendicular to current flow), as displayed in Figure 3b, the behavior is similar to that in B_x , although here the measured magnetic field range is smaller.

To directly inspect the evolution of the spin splitting in a magnetic field along different orientations, the magnetic field is rotated in the x - z plane (Figure 3c) and the x - y plane (Figure 3d) while keeping the amplitude fixed at 1.8 and 1 T, respectively. The magnetoresistance from the adjacent InSb 2DEG increases as the B_z component rises. Thus, after subtracting a constant series resistance at $B_z = 0$ the calculated conductance at finite B_z is lower than the actual value. Consequently, in the regions labeled by 0.5 and 1 in Figure 3c, the quantized plateaus drop below $0.5G_0$ and $1G_0$, respectively (see Supporting Information Figure S5a). A noteworthy feature when the B_z component increases is that both the 0.5 and 1 plateaus widen in V_{SG} . Assuming a constant gate voltage to energy conversion, the Zeeman splitting in the first subband, $E_{1\uparrow-1\downarrow} = |g_1|\mu_B B$ with μ_B as the Bohr magneton, is proportional to the width of the 0.5 plateau along the gate voltage axis.

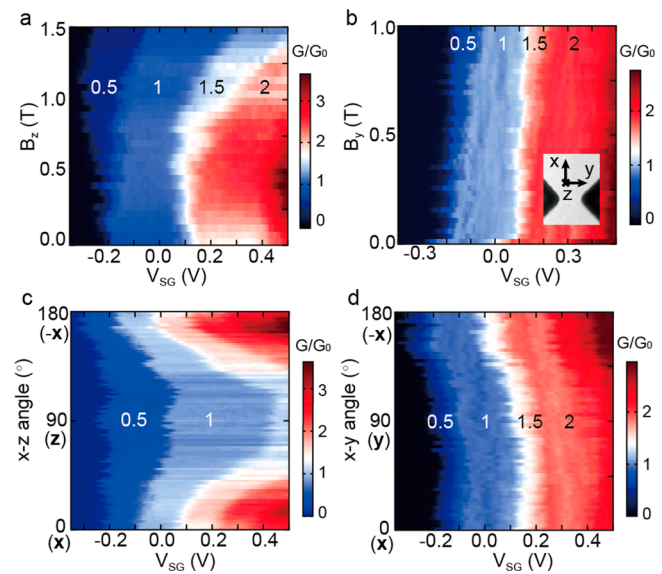


Figure 3. Spin splitting in magnetic fields. (a) G versus V_{SG} and B_z , (b) G versus V_{SG} and B_y , with numbers n marking quantized conductance at nG_0 ($V_{TG} = 0.3$ V). (c,d) G as a function of V_{SG} and the x - z angle at a fixed magnetic field amplitude of 1.8 T (c), and the x - y angle at a fixed magnetic field amplitude of 1 T (d). The x - z angle = 0° , 90° , and 180° correspond to magnetic field along \vec{x} , \vec{z} , and $-\vec{x}$, respectively. Accordingly, in the x - y plane these three angles stand for \vec{x} , \vec{y} , and $-\vec{x}$ directions.

Figure 3c thus shows a g -factor anisotropy up to a factor of ~ 2 between the z and x directions (see Supporting Information Figure S5b). In contrast, the in-plane (x - y plane) g -factor is nearly isotropic as suggested by the roughly constant width of the 0.5 plateau in Figure 3d (see Supporting Information Figure S6a).

To determine the magnitude of the g -factor quantitatively, source-drain bias spectroscopy is performed. Figure 4a-c shows the numerically calculated transconductance dG/dV_{SG} as a function of V_{SG} and V_b at $B_z = 2$ T, $B_z = 1.5$ T and $B_x = 2$ T, respectively, with a fixed $V_{TG} = 0.5$ V. The black dashed lines are guides to the eye and help to read out the energy spacings as marked by the green solid arrows. From $E_{1\uparrow-1\downarrow} = |g_1|\mu_B B$, the effective g -factor for the first subband can be extracted to be $|g_{1,z}| \approx 51$ ($B_z = 2$ T), $|g_{1,z}| \approx 53$ ($B_z = 1.5$ T) and $|g_{1,x}| \approx 26$ ($B_x = 2$ T), exhibiting an anisotropy, as already indicated by Figure 3c. We would like to emphasize that the difference in absolute values between $|g_{1,z}|$ and $|g_{1,x}|$ of ~ 26 is large. Such knowledge of g -factor anisotropy is important for future experiments on helical states and MZMs. One direct consequence is that the Zeeman energy changes differently for different magnetic field orientations. Consistent with Figure 3d, the extracted $|g_{1,y}| \approx 28$ is close to $|g_{1,x}|$, showing a nearly isotropic in-plane g -factor (see Supporting Information Figure S6). In 2D quantum wells, the effective electron g -factor becomes anisotropic due to lower symmetry introduced by the heterostack. It is also renormalized (usually reduced) owing to subband confinement and strain.³⁸⁻⁴¹ The 1D constriction may further modify the effective g -factors, though, the extracted anisotropy is larger than theoretical calculations.^{38,39} Note that the exchange enhancement of the effective g -factor due to the orbital effect of B_z can further modify the anisotropy. The effective g -factor for the second subband can also be obtained from $E_{2\uparrow-2\downarrow}$ giving $|g_{2,z}| \approx 38$ ($B_z = 1.5$ T) and $|g_{2,x}| \approx 23$ ($B_x = 2$ T), both smaller

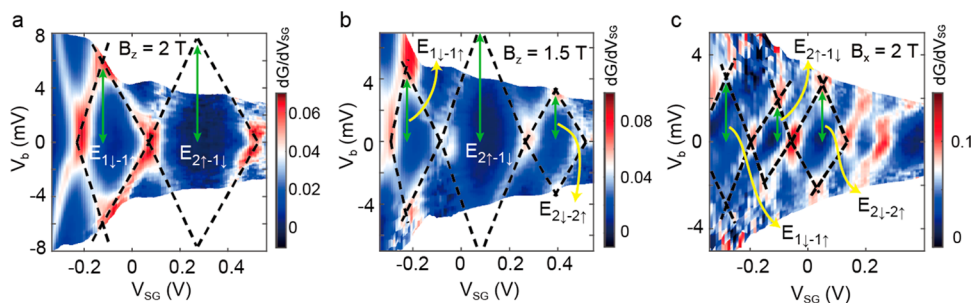


Figure 4. Bias spectroscopy and g -factors. Transconductance dG/dV_{SG} as a function of V_{SG} and V_b at (a) $B_z = 2$ T, (b) $B_z = 1.5$ T, and (c) $B_x = 2$ T with a fixed $V_{TG} = 0.5$ V. The larger dG/dV_{SG} (red color) represents transitions between quantized conductance plateaus. Black dashed lines are guides to the eye and green solid arrows indicate the level spacings.

than the first subband, in qualitative agreement with experimental results on InSb nanowire quantum dots,³ albeit the obtained magnitude of renormalization is somewhat unexpected here. Detailed theoretical discussions are supplied in the Supporting Information (Section III).

Because the extracted g -factor anisotropy of $|g_{1,z}|/|g_{1,x}| \approx 2$ from the bias spectroscopy agrees well with the anisotropy suggested by the width of the 0.5 plateau (ΔV_{SG}) in Figure 3c, the assumption of the constant gate voltage to energy conversion is supported. Therefore, we can use ΔV_{SG} to deduce the g -factor at different angles in the x - z plane. Figure 5a shows the transconductance dG/dV_{SG} of Figure 3c, where

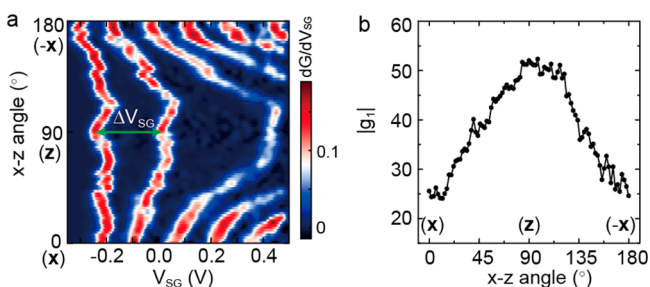


Figure 5. Anisotropic g -factors. (a) Transconductance dG/dV_{SG} extracted as the numerical derivative of the data in Figure 3c. The green arrow indicates the 0.5 plateau width ΔV_{SG} . (b) First subband g -factor $|g_1|$ in the x - z plane calculated based on ΔV_{SG} (see text).

the white-red color represents the transition between conductance plateaus. The green arrow illustrates the width of the 0.5 plateau ΔV_{SG} . The g -factor for the first subband $|g_1|$ can be now obtained from $|g_{1,z}| \times \Delta V_{SG}(\text{angle})/\Delta V_{SG}(\text{angle} = 90^\circ)$ with $|g_{1,z}| \approx 52$. Figure 5b presents the angular anisotropy of $|g_1|$.

Next we turn to magnetic depopulation to extract the electron effective mass. At $B = 0$, the parabolic confinement from the gates (as indicated by the fact that $E_{2,-1} \approx E_{3,-2}$ in Figure 1e) results in subband spacings of $\hbar\omega_0$ ($\hbar = h/2\pi$). When a perpendicular magnetic field (along \vec{z}) is applied, an additional magnetic parabolic potential enhances the level separation to $\hbar\sqrt{\omega_0^2 + \omega_c^2}$, where $\omega_c = eB_z/m^*$ is the cyclotron frequency (m^* is the effective mass).^{34,35,42} Hence, at finite B_z , m^* can be extracted from the subband spacing $E_{2,-1}(B_z) = 1/2E_{1,-1\uparrow} + E_{2,-1\downarrow} + 1/2E_{2,-2\uparrow} = \hbar\sqrt{\omega_0^2 + \omega_c^2}$. Neglecting the orbital effect of B_x , $\hbar\omega_0 \approx 4.7$ meV ($\omega_c = 0$) using the energy intervals in Figure 4c at $B_x = 2$ T ($E_{1,-1\uparrow} \approx 3.0$ meV, $E_{2,-1\downarrow} \approx 1.9$ meV, $E_{2,-2\uparrow} \approx 2.6$ meV). Consequently, the effective mass

is calculated to be $m^* \approx 0.017m_e$ and $0.019m_e$ by applying the energy separations at $B_z = 1.5$ and 2 T, respectively, with m_e the electron mass. More details of the calculation can be found in the Supporting Information (Section II). For an InSb quantum well, confinement enhances the effective mass and the nonparabolicity of the band dispersion enhances it further at finite densities.³⁹ The average m^* of $0.018m_e$ is larger than the bulk value of $0.014m_e$ ¹ but is consistent with theoretical calculations for a 30 nm thick InSb quantum well at low densities.³⁹

In conclusion, we demonstrate a high quality conductance quantization of QPCs on InSb quantum wells. In a rotating magnetic field, Zeeman spin splitting is investigated and a large in-plane and out-of-plane g -factor anisotropy is observed. In a moderate in-plane magnetic field, clear crossings of electron subbands with opposite spins are achieved. Moreover, for the first time, the electron effective mass is extracted from magnetic depopulation of 1D subbands in InSb QPCs. Further research on InSb quantum wells on carefully designed hybrid devices is needed to pursue helical states and Majorana zero modes.

■ ASSOCIATED CONTENT

Supporting Information

The Supporting Information is available free of charge on the ACS Publications website at DOI: 10.1021/acs.nanolett.6b03297.

Extra figures, analysis and theoretical discussions (PDF)

■ AUTHOR INFORMATION

Corresponding Author

*E-mail: L.P.Kouwenhoven@tudelft.nl.

Notes

The authors declare no competing financial interest.

■ ACKNOWLEDGMENTS

We gratefully acknowledge Michal Nowak, Jakob Kamhuber, and Maja Cassidy for very helpful discussions. We would like to thank Jacob Thorp for MBE growth of samples. This work has been supported by funding from The Netherlands Foundation for Fundamental Research on Matter (FOM) and Microsoft Corporation Station Q.

■ REFERENCES

- (1) Vurgaftman, I.; Meyer, J. R.; Ram-Mohan, L. R. *J. Appl. Phys.* **2001**, *89* (11), 5815–5875.
- (2) Lamari, S. *J. Appl. Phys.* **2002**, *91* (3), 1698–1700.

- (3) Nilsson, H. A.; Caroff, P.; Thelander, C.; Larsson, M.; Wagner, J. B.; Wernersson, L.-E.; Samuelson, L.; Xu, H. Q. *Nano Lett.* **2009**, *9* (9), 3151–3156.
- (4) Žutić, I.; Fabian, J.; Das Sarma, S. *Rev. Mod. Phys.* **2004**, *76* (2), 323–410.
- (5) Sau, J. D.; Lutchyn, R. M.; Tewari, S.; Das Sarma, S. *Phys. Rev. Lett.* **2010**, *104* (4), 040502.
- (6) Alicea, J. *Phys. Rev. B: Condens. Matter Mater. Phys.* **2010**, *81* (12), 125318.
- (7) Štředa, P.; Šeba, P. *Phys. Rev. Lett.* **2003**, *90* (25), 256601.
- (8) Mourik, V.; Zuo, K.; Frolov, S. M.; Plissard, S. R.; Bakkers, E. P. A. M.; Kouwenhoven, L. P. *Science* **2012**, *336* (6084), 1003–1007.
- (9) Deng, M. T.; Yu, C. L.; Huang, G. Y.; Larsson, M.; Caroff, P.; Xu, H. Q. *Nano Lett.* **2012**, *12* (12), 6414–6419.
- (10) Das, A.; Ronen, Y.; Most, Y.; Oreg, Y.; Heiblum, M.; Shtrikman, H. *Nat. Phys.* **2012**, *8* (12), 887–895.
- (11) Albrecht, S. M.; Higginbotham, A. P.; Madsen, M.; Kuemmeth, F.; Jespersen, T. S.; Nygård, J.; Krogstrup, P.; Marcus, C. M. *Nature* **2016**, *531* (7593), 206–209.
- (12) Rokhinson, L. P.; Liu, X.; Furdyna, J. K. *Nat. Phys.* **2012**, *8* (11), 795–799.
- (13) Aasen, D.; Hell, M.; Mishmash, R. V.; Higginbotham, A.; Danon, J.; Leijnse, M.; Jespersen, T. S.; Folk, J. A.; Marcus, C. M.; Flensberg, K.; Alicea, J. *Phys. Rev. X* **2016**, *6*, 031016.
- (14) van Heck, B.; Akhmerov, A. R.; Hassler, F.; Burrello, M.; Beenakker, C. W. J. *New J. Phys.* **2012**, *14* (3), 035019.
- (15) Hyart, T.; van Heck, B.; Fulga, I. C.; Burrello, M.; Akhmerov, A. R.; Beenakker, C. W. J. *Phys. Rev. B: Condens. Matter Mater. Phys.* **2013**, *88* (3), 035121.
- (16) Plissard, S. R.; van Weperen, I.; Car, D.; Verheijen, M. A.; Immink, G. W. G.; Kammhuber, J.; Cornelissen, L. J.; Szombati, D. B.; Geresdi, A.; Frolov, S. M.; Kouwenhoven, L. P.; Bakkers, E. P. A. M. *Nat. Nanotechnol.* **2013**, *8* (11), 859–864.
- (17) Goldammer, K. J.; Chung, S. J.; Liu, W. K.; Santos, M. B.; Hicks, J. L.; Raymond, S.; Murphy, S. Q. *J. Cryst. Growth* **1999**, *201*–202, 753–756.
- (18) Orr, J. M. S.; Gilbertson, A. M.; Fearn, M.; Croad, O. W.; Storey, C. J.; Buckle, L.; Emeny, M. T.; Buckle, P. D.; Ashley, T. *Phys. Rev. B: Condens. Matter Mater. Phys.* **2008**, *77* (16), 165334.
- (19) Yi, W.; Kiselev, A. A.; Thorp, J.; Noah, R.; Nguyen, B.-M.; Bui, S.; Rajavel, R. D.; Hussain, T.; Gyure, M. F.; Kratz, P.; Qian, Q.; Manfra, M. J.; Pribiag, V. S.; Kouwenhoven, L. P.; Marcus, C. M.; Sokolich, M. *Appl. Phys. Lett.* **2015**, *106* (14), 142103.
- (20) Rainis, D.; Loss, D. *Phys. Rev. B: Condens. Matter Mater. Phys.* **2014**, *90* (23), 235415.
- (21) Gül, Ö.; van Woerkom, D. J.; Weperen, I. v.; Car, D.; Plissard, S. R.; Bakkers, E. P. A. M.; Kouwenhoven, L. P. *Nanotechnology* **2015**, *26* (21), 215202.
- (22) Khodaparast, G. A.; Doezema, R. E.; Chung, S. J.; Goldammer, K. J.; Santos, M. B. *Phys. Rev. B: Condens. Matter Mater. Phys.* **2004**, *70* (15), 155322.
- (23) Khodaparast, G. A.; Meyer, R. C.; Zhang, X. H.; Kasturirachchi, T.; Doezema, R. E.; Chung, S. J.; Goel, N.; Santos, M. B.; Wang, Y. J. *Phys. E* **2004**, *20* (3–4), 386–391.
- (24) Kallaher, R. L.; Heremans, J. J.; Goel, N.; Chung, S. J.; Santos, M. B. *Phys. Rev. B: Condens. Matter Mater. Phys.* **2010**, *81* (7), 075303.
- (25) Gilbertson, A. M.; Fearn, M.; Jefferson, J. H.; Murdin, B. N.; Buckle, P. D.; Cohen, L. F. *Phys. Rev. B: Condens. Matter Mater. Phys.* **2008**, *77* (16), 165335.
- (26) Leontiadou, M. A.; Litvinenko, K. L.; Gilbertson, A. M.; Pidgeon, C. R.; Branford, W. R.; Cohen, L. F.; Fearn, M.; Ashley, T.; Emeny, M. T.; Murdin, B. N.; Clowes, S. K. *J. Phys.: Condens. Matter* **2011**, *23* (3), 035801.
- (27) Gilbertson, A. M.; Branford, W. R.; Fearn, M.; Buckle, L.; Buckle, P. D.; Ashley, T.; Cohen, L. F. *Phys. Rev. B: Condens. Matter Mater. Phys.* **2009**, *79* (23), 235333.
- (28) van Weperen, I.; Tarasinski, B.; Eeltink, D.; Pribiag, V. S.; Plissard, S. R.; Bakkers, E. P. A. M.; Kouwenhoven, L. P.; Wimmer, M. *Phys. Rev. B: Condens. Matter Mater. Phys.* **2015**, *91* (20), 201413.
- (29) Nitta, J.; Akazaki, T.; Takayanagi, H.; Enoki, T. *Phys. Rev. Lett.* **1997**, *78* (7), 1335–1338.
- (30) Uddin, M. M.; Liu, H. W.; Yang, K. F.; Nagase, K.; Sekine, K.; Gaspe, C. K.; Mishima, T. D.; Santos, M. B.; Hirayama, Y. *Appl. Phys. Lett.* **2013**, *103* (12), 123502.
- (31) Kammhuber, J.; Cassidy, M. C.; Zhang, H.; Gül, Ö.; Pei, F.; de Moor, M. W. A.; Nijholt, B.; Watanabe, K.; Taniguchi, T.; Car, D.; Plissard, S. R.; Bakkers, E. P. A. M.; Kouwenhoven, L. P. *Nano Lett.* **2016**, *16* (6), 3482–3486.
- (32) de la Mata, M.; Leturcq, R.; Plissard, S. R.; Rolland, C.; Magén, C.; Arbiol, J.; Caroff, P. *Nano Lett.* **2016**, *16* (2), 825–833.
- (33) Goel, N.; Graham, J.; Keay, J. C.; Suzuki, K.; Miyashita, S.; Santos, M. B.; Hirayama, Y. *Phys. E* **2005**, *26* (1–4), 455–459.
- (34) van Wees, B. J.; Kouwenhoven, L. P.; van Houten, H.; Beenakker, C. W. J.; Mooij, J. E.; Foxon, C. T.; Harris, J. J. *Phys. Rev. B: Condens. Matter Mater. Phys.* **1988**, *38* (5), 3625–3627.
- (35) Berggren, K. F.; Thornton, T. J.; Newson, D. J.; Pepper, M. *Phys. Rev. Lett.* **1986**, *57* (14), 1769–1772.
- (36) Graham, A. C.; Thomas, K. J.; Pepper, M.; Cooper, N. R.; Simmons, M. Y.; Ritchie, D. A. *Phys. Rev. Lett.* **2003**, *91* (13), 136404.
- (37) van Weperen, I.; Plissard, S. R.; Bakkers, E. P. A. M.; Frolov, S. M.; Kouwenhoven, L. P. *Nano Lett.* **2013**, *13* (2), 387–391.
- (38) Winkler, R. *Spin-Orbit Coupling Effects in Two-Dimensional Electron and Hole Systems*; Springer-Verlag: Berlin, 2003.
- (39) Nedniyom, B.; Nicholas, R. J.; Emeny, M. T.; Buckle, L.; Gilbertson, A. M.; Buckle, P. D.; Ashley, T. *Phys. Rev. B: Condens. Matter Mater. Phys.* **2009**, *80* (12), 125328.
- (40) Kiselev, A. A.; Kim, K. W.; Ivchenko, E. L. *Phys. Status Solidi B* **1999**, *215* (1), 235–239.
- (41) Ivchenko, E. L.; Kiselev, A. A. *Soviet Physics Semiconductors-Ussr* **1992**, *26* (8), 827–831.
- (42) Beenakker, C. W. J.; van Houten, H. *Quantum Transport in Semiconductor Nanostructures*. In *Solid State Physics*; Henry, E., David, T., Eds. Academic Press: New York, 1991; Vol. 44, pp 1–228.